Force enhanced wire laser additive manufacturing of aluminum and titanium alloys

Zhe Zhao [a], Shuoheng Xu[a], Jian Liu[a], Xiaohan Zhang[a], Min Xia[c*], Yaowu Hu [a, b*]

[a] The Institute of Technological Sciences, Wuhan University, Wuhan, 430072, China

[b] School of Power and Mechanical Engineering, Wuhan University, 430072 Wuhan, China

[c] Department of Engineering, Lancaster University, Lancaster, LA1 4YW, United Kingdom

*Corresponding author: Yaowu Hu, Min Xia

E-mail: yaowuhu@whu.edu.cn,m.xia3@lancaster.ac.uk

Abstract

Brittle intermetallic compound formation is typically difficult to avoid during fusion joining of dissimilar metals. In this paper, a new approach called force enhanced wire laser additive manufacturing is proposed to join aluminum and titanium alloys. Ti6Al4V titanium alloy single track was additively fabricated on AA7075 plate successfully, through two liquid pools of the wire and the substrate, separated by a buckled unmelted part of the wire, leading to a mechanically interlocked interface. The effects of manufacturing parameters including laser power, wire feeding speed, scanning speed and initial contact force between wire and substrate on the surface morphology, internal interface microstructure and formation of intermetallic compounds were investigated through high-speed camera, spectrometer, laser topography, optical imaging, SEM imaging, XRD characterizations along with numerical simulations at different scales. And the maximum tensile strength reached 380MPa in the tensile test. The experimental and numerical results indicate that the thermal modulation approach can effectively control the formation of brittle compounds between titanium and aluminum alloys and that the initial contact force ensures a good bond between the two metals.

Keywords: Force enhanced; Laser additive manufacturing; Titanium; Aluminum

1. Introduction

Additive manufacturing (AM), commonly referred to as 3D Printing, produces target parts by repeated layer deposition, based on the three-dimensional data [1]. In the past decades, AM technology has been developed rapidly as a key technology that can completely change the manufacturing industry and can quickly manufacture objects with complex and customized geometries that cannot be easily and economically produced by conventional methods [2–6]. AM technology can achieve complex internal lattice structures and maintain the overall strength of the part by reducing the density and using a thicker grid in the low stress bearing area, while greatly reducing its weight [7]. Additionally, AM is promising to control and tune the microstructure of the target product and the mechanical properties of the printed structure [6,8,9]. The metal AM industry has seen a significant surge in different advanced printing technologies and devices [10]. However, printing metals at dissimilar interfaces is still challenging due to brittle intermetallic compound formation, thermal stresses, and other issues because of the significant differences in physical and chemical properties of dissimilar metals.

Multiple methods have been recently developed for joining dissimilar interfaces. Dissimilar metals can be joined in solid state through friction stir welding, where metals are plastically deformed and inter-connected under high temperature [11–16]. In this case, the materials will not

form new phases and the formation of brittle alloy compounds is prohibited. He et al. [17] systematically reviewed the numerical analysis of various aspects during the welding process, including the effects of grain size, heat and thermo-mechanically affected zones, residual stress and mechanical properties of the joints. However, this method needs a pin and generates large plastic deformation area around the pin, which limits the precision of the process. The final pin hole also needs additional treatment. Furthermore, incorporating a friction stir device in additive manufacturing systems is cumbersome and economically unfriendly. Another method for joining dissimilar interfaces is through an inserted third material [18–22]. This method is effective only if a proper interlayer can be found. For instance, Gao et al. [23] pointed out that the excessive heat input at the Ti weld interface produced an excess of brittle Mg17Al12 that led to fracture at this interface during the tensile test in the research of joining Ti alloy and steel with Mg as the interlayer. Tomashchuk et al. [24] utilized electron beam to weld titanium alloy and stainless steel via copper as the interlayer and they found that the mechanical stability of the welded joint largely depends on the thickness of the intermetallic layer. Therefore, finding an appropriate interlayer is crucial to produce the required mechanical properties but difficult in practice. The process also creates two additional dissimilar interfaces which increase the thickness of the interface. Given the limitations, these methods haven't been widely applied in industry. Besides the aforementioned methods, Zhao et al. [25] studied brazing behavior in joining lead and titanium alloy with the weld pool majority in lead. Brazing can now be carried out by hot pen, ultrasonic, laser, arc and many other heat sources. Despite the development of brazing techniques and their use in manufacturing practice, brazing results in sharp material interfaces and the interaction of the materials is weak.

Dissimilar metals joined at liquid state should have better properties and many researchers have investigated the heat and mass transport phenomena, microstructures, and mechanical properties. Yao et al. [26] studied the interface microstructure and mechanical properties of laser welding copper-steel combination and they demonstrated that the stability of the joint could be improved by controlling the amount of copper dissolved in the steel melt pool. Hu et al. [27]reported that both heat and mass transport are significantly influenced by convection during laser spot welding of stainless steel and nickel. Appropriate heat control is used to join carbon steel and aluminum alloy by laser beam. Preheating is usually adopted to control the stress levels. Liquid state mixing is generally believed to be the better choice [28,29].

Here we join two metals with buckled solid interface, and show metals with distinct physical properties (melting point difference exceeds 1000 K; thermal conductivity difference exceeds 19 times) like titanium alloy and aluminum alloy can be additively manufactured with minimum intermetallic compound formation through a new approach called force enhanced wire laser additive manufacturing (FEWLAM). We add titanium wire to aluminum substrate in this process to benefit from the light absorbent property of titanium to make the process more energy efficient. Force is exerted on the wire to introduce buckling of the partially melted wire to introduce mechanical interlocking of the two separated weld pools. High speed camera and optical spectrometer are used to monitor the additive process. Optical and scanning electron microscopies (SEM) are used to characterize the joint interface. X-rays diffraction (XRD) analysis is carried out to illustrate the chemical bond formation. We use finite volume method modeling based on our previous research to simulate the heat and mass transport in the two weld pools. The interface formation mechanism between the two weld pools is studied by molecular dynamics simulations. This study is the first work that uses wire buckling to assist dissimilar joining process, to the best of the authors'

knowledge, and it provides an additional joining mechanism, for difficult-to-join conditions.

2. Experimental procedure

In this study, 7075 Aluminum alloy was selected as substrate material (100mm×20mm×5mm) and its chemical composition is shown in Table I. The wire material was aviation-grade Ti6Al4V alloy bar with a diameter of 1.2 mm and its chemical composition is shown in Table II.

Table I Chemical composition of 7075 Aluminum alloy (wt.%)

Zn	Mg	Cu	Mn	Ti	Cr	Si	Fe	Al
5.23	2.10	1.45	0.30	0.16	0.23	0.22	0.22	Bal

Table II Chemical composition of Ti6Al4V alloy (wt. %)

Al	V	Fe	O	C	H	N	Ti
6.270	4.080	0.048	0.021	0.020	0.004	0.031	Bal

The FEWLAM setup used in the research is shown in **Fig. 1**. A 1000W laser device (MFSC-1000W, Shenzhen Chuangxin Laser Co., Ltd.) is used as the heat source to melt the metallic wire. The oil and dust on the surface of the substrates were wiped with alcohol and acetone, and then dried. Finally, the aluminum alloy substrate was fixed with fixture. Ti6Al4V alloy wire was fed by the wire feeding machine (BWT16). An optical spectrometer (CCS100/M) is used to collect optical spectral information during the experiment process. The optical spectrometer has a wavelength range of 350–700 nm and a resolution $\Delta\lambda < 0.5$nm and its sampling frequency is 10Hz. The spectral information is sent to the computer by the data cable. The computer is connected to a 3-axis CNC machine for control of the direction and speed of movement of the substrate. The high-speed camera (CHRONOS) was used to collect the pictures during manufacturing. The sampling rate used in this study was 1057 frames/s. The size of the captured image is 1280×1024 pixels. A 405nm laser is equipped as auxiliary lighting to illuminate the melt-pool surrounding and a 405 nm filter is mounted in front of the high-speed camera to reduce the impact of melt-pool irradiations. The shielding gas was 99.9% argon with pressure of 0.25MPa.
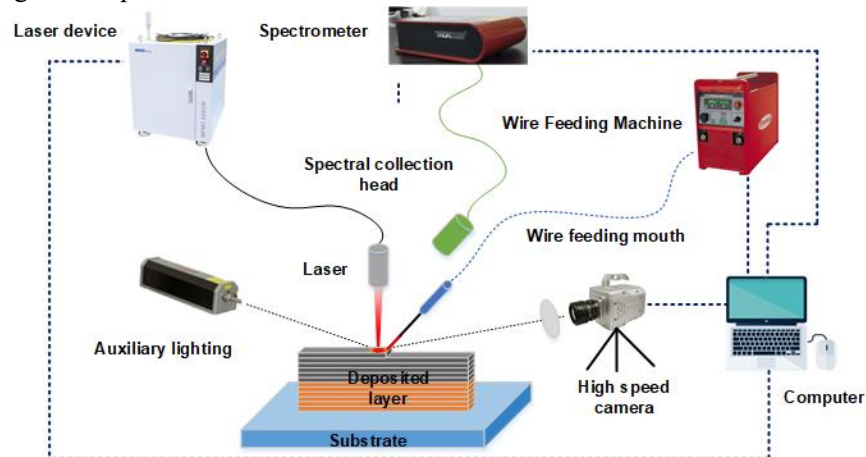
Fig. 1. Schematic setup of FEWLAM experiment process.

The cross sections of Al-Ti samples were polished by using silicon carbide sandpapers of different grades: 200, 400, 1000, 2000 and 3000. and diamond pastes (2.5 μm ,1 μm and 0.5 μm). Then samples were observed by an Olympus-BX51 (OLYMPUS, Japan) optical microscope (OM). For better microstructure visualization, the samples were corroded by Keller's reagent (2.5ml HNO_3, 1.5ml HCl, 1ml HF and 95ml H_2O) for 30s, and cleaned by acetone, analyzed with a VHZ-1000E OM. Then, SEM (Tescan, The Czech Republic) or optical microscope was used to observe the

microstructure. The elemental composition of the melt track was analyzed using EDS (Aztec Energy, Oxford Instruments Nanoanalysis) with the line and area scanning models. Samples were tested on an electronic universal testing machine (QLW-50S, XiaMen Group Lung Instrument Co., LTD). The standard for tensile testing is the National Standard of the People's Republic of China GB/T228.1-2010.

3. Methodology

Fusion joining of two metals typically involves melting of both metals and their mixing at liquid state. For powder bed fusion additive manufacturing, the laser selectively melts the powder resulting in direct contact between the melt pools of the two metals, which tends to produce more brittle intermetallic compounds, resulting in much weaker joining properties between dissimilar materials. Brazing also usually leads to a weaker joining interface and significant material separation. For titanium and aluminum alloys, if both metals are completely melted, significant mixing and spattering will occur due to the difference in physical properties of the two metals, and intermetallic compounds will form, impacting the mechanical properties of the joint.

FEWLAM distinguishes itself from other wire additive processes by two important characteristics: force-enhanced interfacial biting and liquid guiding. Without the ultrathin solid interface, interface bite would not be possible. And melt will form droplet under the influence of surface tension. The realization of FEWLAM is dependent on the process parameters such as laser power, wire feeding speed and scanning speed, and also the contact force (horizontal component), which is the main difference from traditional methods. The contact force between the Ti wire and the Al alloy substrate ensures that during the FEWLAM process the metals are in firm contact and buckling occurs at the solid phase which is between two liquid phases.

In this research, the angle between wire material and substrate material is controlled to be 35°-55 °, and the initial contact force F_z between the wire and the substrate in the vertical direction is controlled at 1.8 N-2.7 N to ensure the interfacial contact between dissimilar metals. This ensures good heat transfer between dissimilar metals. The force is modulated through external vibrator. As shown in **Fig. 2**(a), with temperature difference between two materials, heat is transferred from the upper region of the titanium alloy to the interior of the aluminum alloy, and the upper region of the aluminum alloy in direct contact with the titanium alloy undergoes partial melting.

Figs. 2(b-f) shows the evolution of the temperature fields with two melt pools and thin solid Ti alloy region between them. It can be seen that within the first 0.5 seconds of laser irradiation, the temperature quickly reaches the melting point of the titanium wire. Under a firm thermal contact with the aluminum plate which is highly thermal conductive, the titanium wire will not be completely melted, as the melting temperature of Al alloy is lower than that of Ti alloy. The temperature field as shown in **Fig. 2**(f) shows the mechanism of the formation of two melt pools.

Molecular dynamics simulations: first select the appropriate initial conditions, including the initial position, initial velocity, time step and so on. Set shrink-wrapped boundary conditions in x, y and z directions. The time step is 1 fs. **Fig. S1** shows the initial Al-Ti model based on Large-scale Atomic/Molecular Massively Parallel Simulator (LAMMPS) software. There are 83776 Al atoms and 7609 Ti atoms in the system (Lattice αAl = 0.405 nm and αTi = 0.295 nm). The simulation process is carried out under NVT ensemble. The initial Al-Ti model is firstly equilibrated at 500 K in the NVT ensemble for 4ps. Then quickly raise the temperature of the melt pool to 1400 K. After that, keep this temperature for 10 picoseconds and record the atomic diffusion at the Al-Ti interface. In order to verify the effect of Ti wire force, an oblique downward force along the Ti wire is added

4

to the area of Ti atoms when the melt pool area just reaches the target temperature. The details of the finite volume method are given in the supplementary information. The material properties used are shown in Table III.
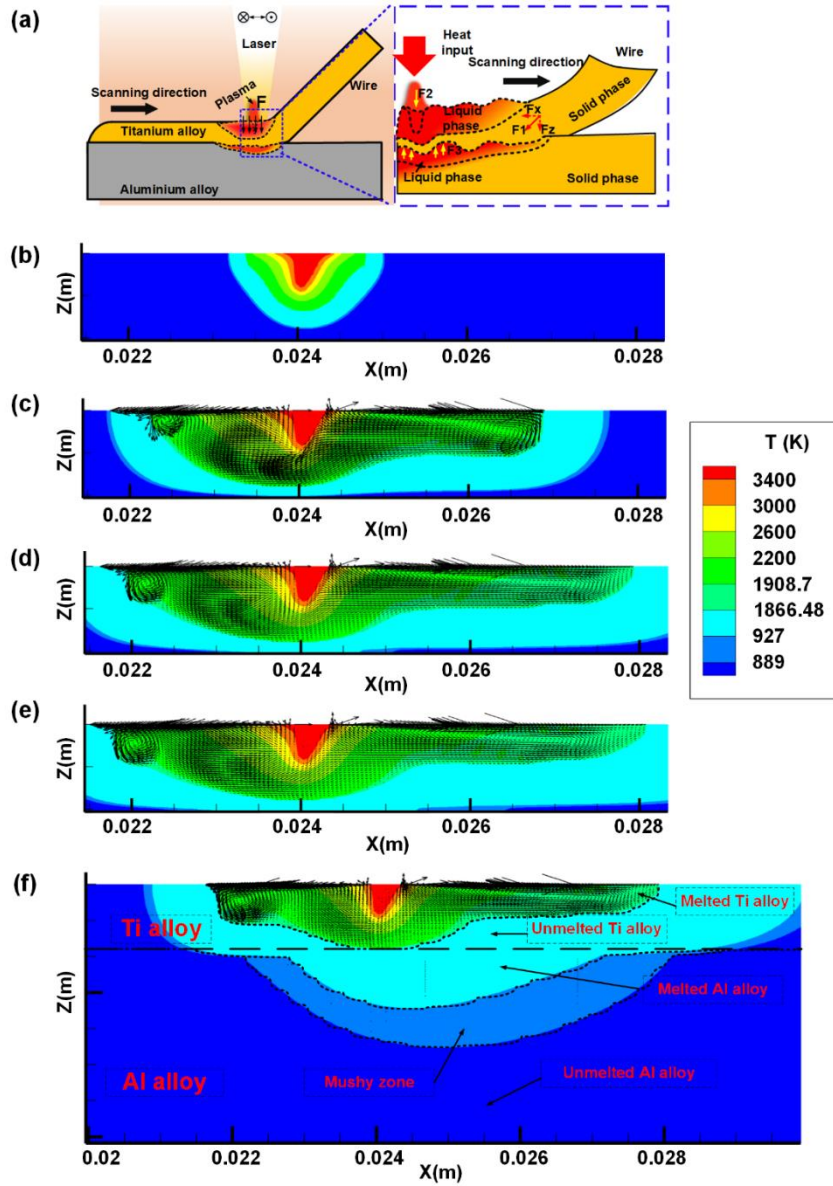
Fig. 2. Technical schematic diagram and finite volume modeling of the FEWLAM strategy based on the interface buckling behavior. (a) Schematic diagram of stress and melt pool distribution of wire and substrate. (b-e) Evolution of temperature fields at the titanium layer at 0.01 s, 0.25 s, 0.5 s, and 1 s. (f) Temperature field and flow behavior at steady state. The Liquidus and the solidus lines show the melt boundary of the aluminum alloy. The dashed line shows the interface of titanium alloy and aluminum alloy.

Table III Material properties used in the simulation [30,31]

Property/parameter	Ti6Al4V	AA7075
Density of liquid metal (kg m^{-3})	4510	2810
Dynamic viscosity (kg m^{-1} s^{-1})	3.4×10^{-3}	1.2×10^{-3}
Solidus temperature (K)	1886.48	753
Liquidus temperature (K)	1908.70	917

|		
Specific heat of solid (J kg^{-1}K^{-1})	560	870
Specific heat of liquid (J kg^{-1}K^{-1})	1126	900
Effective thermal conductivity of solid (W m^{-1} K^{-1})	6.8	130
Surface tension (N m^{-1})	1.64	0.868
Temperature coefficient of surface tension (N m^{-1} K^{-1})	-2.8×10^{-4}	-3.5×10^{-4}
Coefficient of thermal expansion (K^{-1})	1.1×10^{-5}	2.34×10^{-5}
Latent heat (J kg^{-1})	4.1×10^{5}	3.8×10^{5}
Effective mass diffusivity (m^2 s^{-1})	5×10^{-3}	5×10^{-3}

4. Result and discussion

4.1 Comparison of force enhancement and no force enhancement

Finite volume modeling is carried out to illustrate the heat and mass transport with and without force enhancement of the process. **Fig. 3** shows the temperature fields and fluid behavior at and near the melt pool without force enhancement, where a 0.2 mm interfacial thermal barrier with lower conductivity was set to simulate the contact between titanium melt and the aluminum plate. It should be noted that such a setting is reasonable because titanium melt region tends to form droplets under the influence of its surface tension, reducing the contact area between these two. The melt pool and high temperature region in **Fig. 3**(a) and (c) are significantly larger than those shown in **Fig. 3**(b) and (d), as a consequence of heat transport due to the aluminum plate. The large liquid pool without force enhancement will further generate poor thermal interfaces, leading to fragile bonding between aluminum alloy and titanium alloy. In **Fig. 3**(b, d), the titanium wire is only partially melted near the contact point of the wire and plate, which holds the shape of the titanium alloy liquid and ensures the contact between the two metals. Under proper processing parameters, a solid portion could be preserved, inhibiting severe liquid mixing and intermetallic compound forming. To further demonstrate the interface interlocking mechanism of FEWLAM compared to traditional approach, molecular dynamics simulations using LAMMPS are carried out. **Fig. 4** shows simulation results of the titanium alloy wire additively manufactured on top of aluminum alloy without and with the introduction of lateral forces on the wire which induces mechanical deformation of the hot solid area between two melt pools. Such a mechanical force introduces bulking and perturbations at the interface, as shown in **Fig. 4**(b) where the aluminum atoms move across the boundary into the titanium area, leading to interlocked and stronger mechanical bonding between the two alloys. The temperature profiles of melt pool are shown in **Fig. S1**, showing no significant temperature rise due to the introduction of the force. In practice, as the interaction of aluminum and titanium is weak, the titanium melt will detach from aluminum, leading to joining failures, as shown in **Figs. 4**(c-d). Due to the detachment, the melt size would be much larger in **Fig. 4**(c), agreeing with simulation result in **Fig.2** and **3**.

The contact force F_1 can be decomposed into horizontal force F_x, which is opposite to the scan direction, and vertical force F_z, which is perpendicular to the scan direction. The horizontal force F_x ensures the supply of the wire along the horizontal direction. The supporting force F_3, the recoil pressure F_2, and the vertical force F_z provide the squeezing action along the vertical direction for the solid wire and the molten pool of the substrate, ensuring good penetration of the wire in the substrate melt pool for an excellent joining of dissimilar metals. As shown in **Fig. 4**(e), due to insufficient initial contact force, the interaction of Al alloy and Ti alloy is weak, resulting in poor mechanical properties of the joint. One example of the cross-section for the case with force

enhancement is shown in **Fig. 4**(f) and will be discussed further.
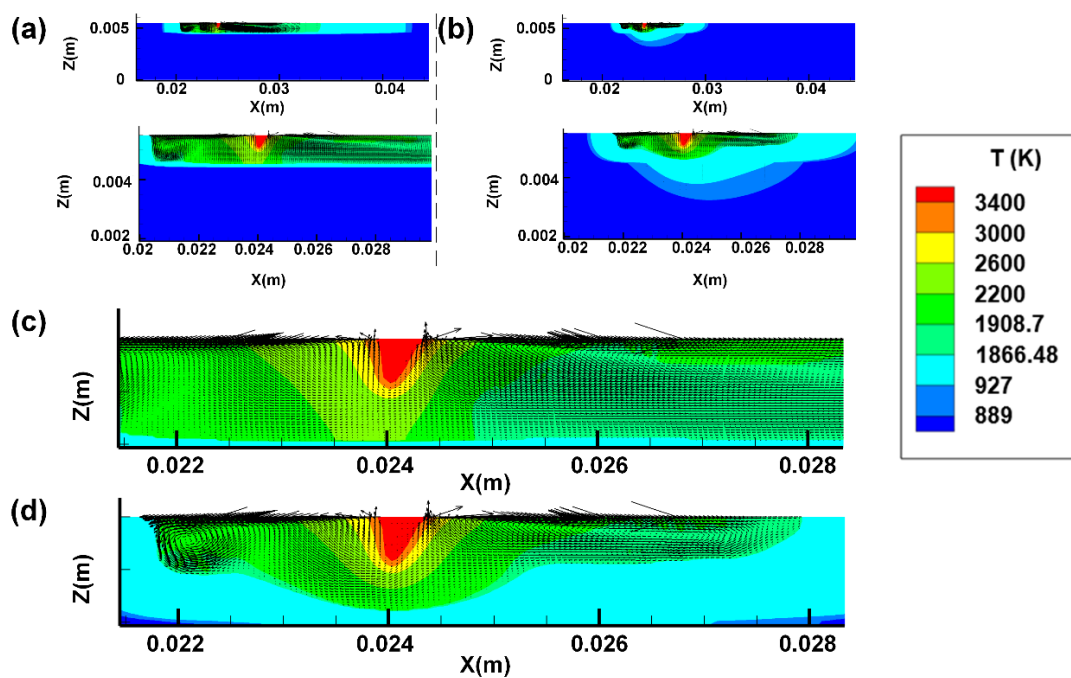
Fig. 3. Comparison of the temperature fields and flow behavior between two cases at steady states and different magnifications: without force enhancement between titanium alloy and aluminum (a, c), and with force enhancement case (b, d).
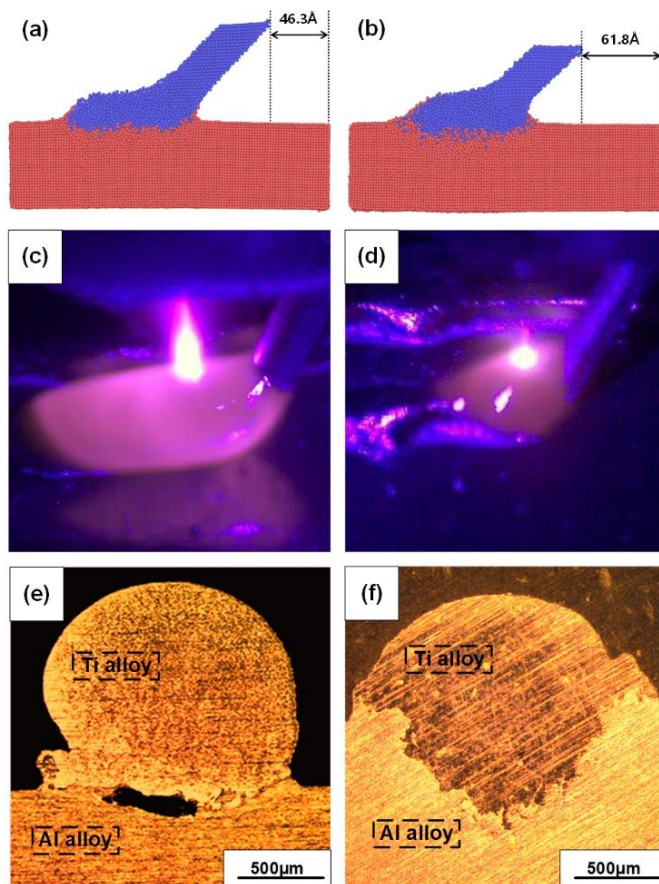
Fig. 4. Comparison of traditional method and FEWLAM with lateral force. Molecular dynamics

simulation of interface forming in traditional additive manufacturing (a) and FEWLAM (b). Blue represents titanium and red is aluminum. Other parameters are kept the same. Process monitoring with interface detaching in traditional method (c) and FEWLAM (d). OM cross sectional images of samples without force enhanced (e) and with force enhanced (f).

With the force at the initial contact condition, we categorize the dissimilar additive process of FEWLAM into several states. When the laser power is too low, the titanium wire is only melted at the top, and the aluminum is still in solid phase, leading to connection failures. However, when the laser power is too high, the titanium wire will completely melt, and the Ti pool directly contact with the aluminum melt pool to form a large number of intermetallic compounds due to the low miscibility of Al and Ti atoms. At the same time, the higher energy input leads to a perturbation of the melt pool, resulting in a large amount of splashing and roughing of the sample surface. Therefore, during our experiment, we control the laser power at 400-800w and the wire feeding speed at 30mm/s-80mm/s, and analyze the four states in this range. We experimentally studied various parameters as shown in Table SI.

4.2 Process parameters analysis

The additive process is monitored by high-speed camera in real time and laser surface topography is used to characterize the added track of titanium, as shown in **Fig.5**. The experimental parameters for the four states are shown in Table IV. It is found that when the heat input is far from being sufficient (state 1), discontinuous tracks can be observed, due to weak interactions between the titanium and the substrate. With increasing laser power and wire feeding rate, most parts of the track become continuous. And under our optimized condition, a complete continuous track is obtained. When the laser power is further increased, the surface becomes rugged but continuous as shown in **Fig. 5**(d). It is shown in **Fig. 5** that the sizes of the melt areas are different, with state 4 being the smallest and state 1 and state 2 being the largest. It is intriguing that state 4 actually has the largest laser power. However, most of the energy goes to the sputtering droplets and the laser penetrates the aluminum rather than being absorbed due to the highly reflective nature of aluminum at this wavelength. With this characteristic, we can distinguish the state of laser manufacturing. While in state 1 and state 2, the contact between the titanium wire, which is thermally less conductive, and the aluminum plate is with thermal barriers. This results in a larger melt pool, as the heat cannot be transported away from the laser irradiating area.

Table IV Experimental parameters of 4 states

Laser Power (W)	Wire feeding speed (mm/s)	Scanning speed (mm/s)	State
400	40	4.17	State 1
500	60	12.5	State 2
550	60	12.5	State 3
800	60	12.5	State 4

The spectral information monitored in the process can also be used to categorize the state of the manufacturing, as shown in **Fig. 6**. The intensity of the peaks increases as the laser power increases. Due to saturation, the spectral intensity in this band will not exceed 360 a.u. We have analyzed the intensity of line Ti I 453.324 nm at different times by combining high-speed cameras, and it is believed that Ti alloys has melted when the intensity of line Ti I 453.324 nm reaches 360 a.u. For state 1, the intensity of line Ti I 453.324 nm is unstable throughout the process and decreases significantly at t=2.7s and t=4.9s, which reflects that the surface of the substrate cannot be melted

due to the lower heat input and the wire does not been stacked on the substrate during this time, which corresponds to the surface of state 1. The intensity of line Ti I 453.324 nm in state 2 is significantly more stable than in state 1 as shown in **Fig. 6**(b), which means that the heat input is able to melt the substrate well enough to allow the unmelted wire to infiltrate the substrate melt pool. However, at t=2.3s and t=3.0s a significant peak drop can be observed, indicating that the Ti wire and substrate are not well bonded at this stage. In contrast, the intensity of line Ti I 453.324 nm in state 3 remained stable after the initial melting, which means that the heat input was able to melt the substrate while melting the wire and keep part of the wire unmelted to prevent direct contact between the melt pools of the two metals. As shown in **Fig. 6**(d), the intensity of line Ti I 453.324 nm was less stable throughout the process than in states 2 and 3 because of the high heat input in state 4, which caused the complete melting of the wire and the direct contact between the two metals, and the explosion of the melt pool in the time period of t=1.3s-2.1s, which resulted in a large amount of spatter and a small melt pool with a large amount of brittle intermetallic compounds.
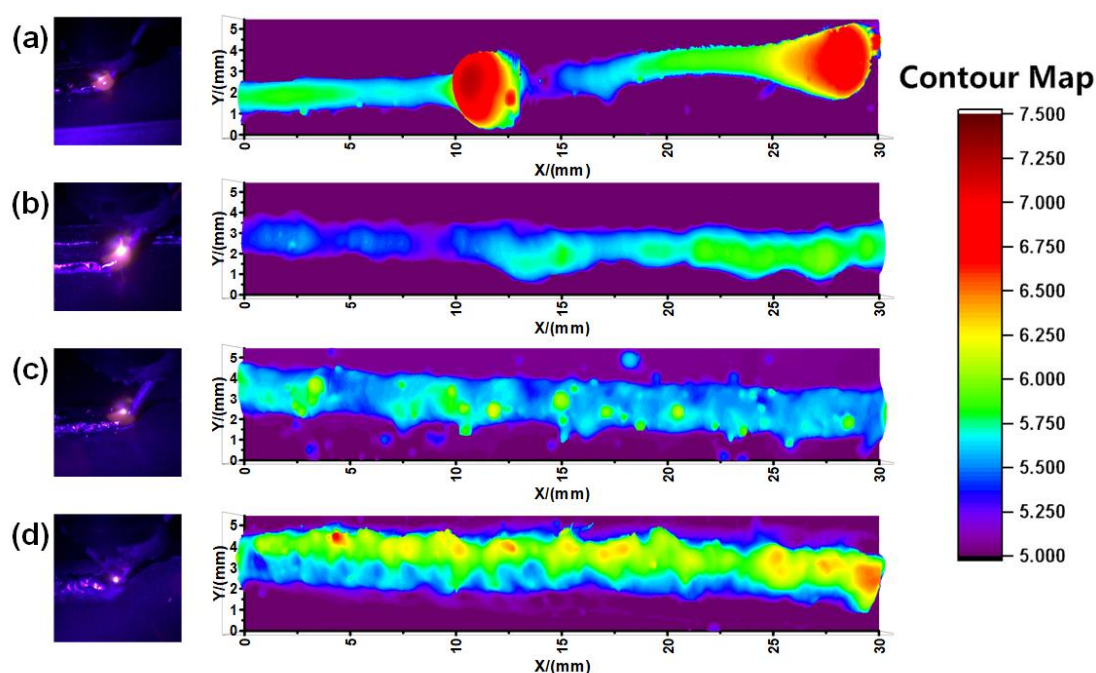

Fig. 5. Surface topography of the four states of FEWLAM: (a) state 1 with discontinuous melt track, (b) state 2 with seldomly occurred discontinuity, (c) state 3 with continuous track, (d) state 4 with large surface variations.

4.3 Microstructure and chemical composition of FEWALAM samples

The melt pool of Al alloy and Ti alloy is separated by the unmelted Ti alloy as shown in **Fig. 7**(a). Under force enhancement and thermal coupling, the unmelted Ti alloy forms an irregular boundary with the Al alloy melt pool, which prevents the formation of Al/Ti intermetallic compounds and improves the interfacial bonding properties. **Figs. 7**(b-e) show the microstructure of the melted and unmelted regions of the Al alloy and the titanium alloy. No obvious martensitic structure is observed between the dashed lines in **Fig. 7**(e), which confirms that this part of the titanium alloy is not melted and is consistent with **Fig. 2**(f).
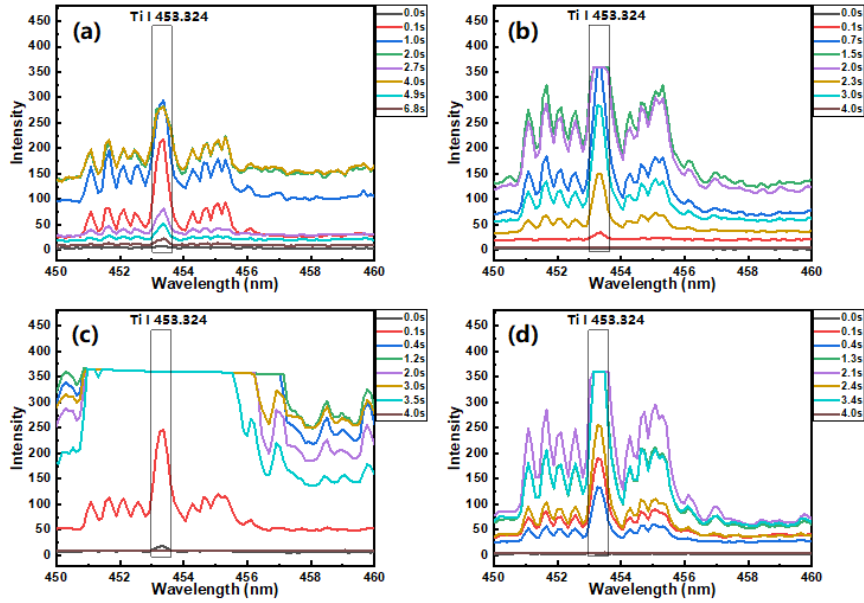
Fig. 6. Spectral information of the four states collected by the optical spectrometer. (a) state 1, (b) state 2, (c) state 3, (d) state 4.
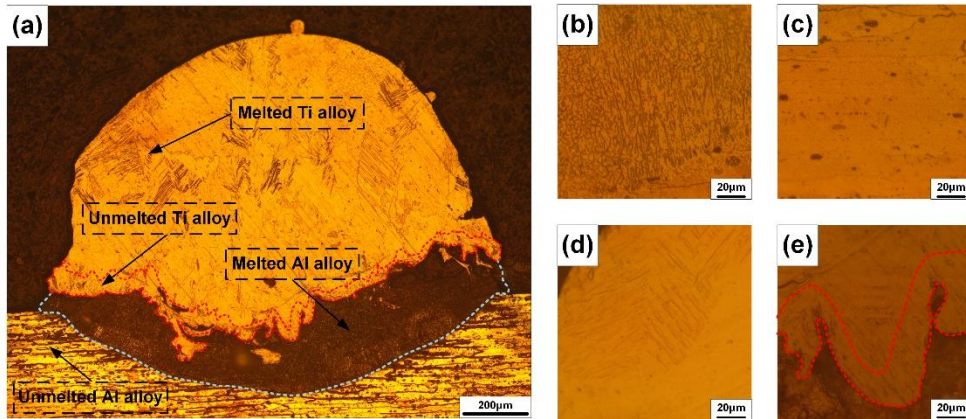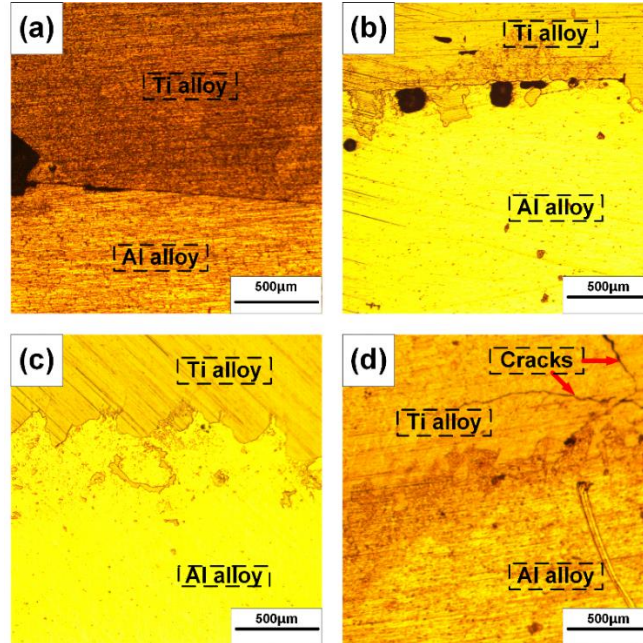

Fig. 7 OM Cross-sectional images of the formed interface. (a) microstructure of the cross section, (b) microstructure of melted Al alloy, (c) microstructure of unmelted Al alloy, (d) microstructure of melted Ti alloy, (e) microstructure of unmelted Ti alloy.

To verify the effect of parameter regulation on the interface, microstructures in different states are collected as shown in **Fig. 8**. For state 1, the melt pool of aluminum cannot infiltrate the Ti wire effectively, and eventually the titanium wire will break away from the substrate due to the heat transferred from the wire to the substrate is too little. The interface could be more interlocked as shown in **Fig. 8**(b), but there are still some areas where the titanium wire and substrate are not bonded which is consistent with the spectral monitoring. **Fig. 8**(c) indicates that two metals have completely interlocked. Such interlocking is an effect due to the combination of mechanical interlocking and metallurgical intermetallic bond forming. **Fig. 8**(d) shows that hot cracks are easily formed under severe heating and intermetallic.

To further distinguish the difference between state 2 and state 3, we focus on the morphology and element distribution at the Ti/Al interface. The SEM images of the interface for state 2 and state 3 are shown in **Fig. 9** and the aluminum area can be clearly distinguished. The titanium area

is shown in the white area and the darker area is aluminum. Intermetallic area is with color in between. The state 2 has both straight line interface and wavy interface, while the interfaces in state 3 are mainly curved ones. This can be resulted from the mechanical force induced deformations or buckling of the interface between the two metals, the mechanism of which will be further investigated in the following part.


Fig. 8. OM Cross-sectional images of the formed interface for the four states: (a) state 1 with no sound interface, (b) state 2 with partial interface locking, (c) state 3 with continuous mechanical and metallurgical bonds, (d) state 4 at the melt pool-heat affected zone showing intermetallic induced hot cracks.
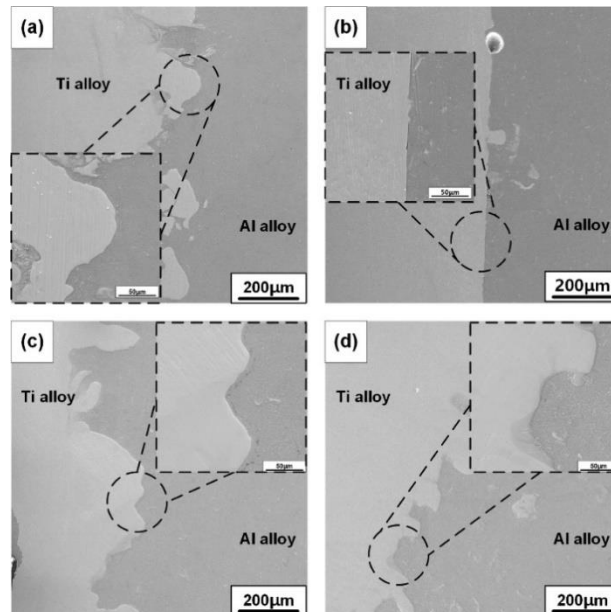
Fig. 9. SEM images of the interfacial morphologies of state 2 (a-b) and state 3(c-d).

We used EDS line scans and XRD to investigate the elemental distribution at the interface and the possible presence of intermetallic compounds. As shown in **Figs. 10** (a-b), the distribution of elements at the interface is sharp for both states 2 and 3. Al is predominantly in the Al alloy, with

only a slight contribution to the Ti alloy, while Ti is only in the Ti alloy. In some parts of the joints in state 3 we observe some Ti and Al compounds with a predominance of both elements, but the main part of the interface is still interlocking mechanical bonds. It is clear from **Figs. 10**(c-e) that these peaks are predominantly from Al and Ti. **Fig. 10**(f) shows clear peaks from AlTi and Al3Ti, compounds that are typically hard and brittle and will significantly affect the mechanical properties of the joint. This suggests that optimisation of the process parameters can be achieved to modulate the heat input and reduce the formation of brittle intermetallic compounds while achieving a complete interlocking of the Ti and Al alloy interfaces.
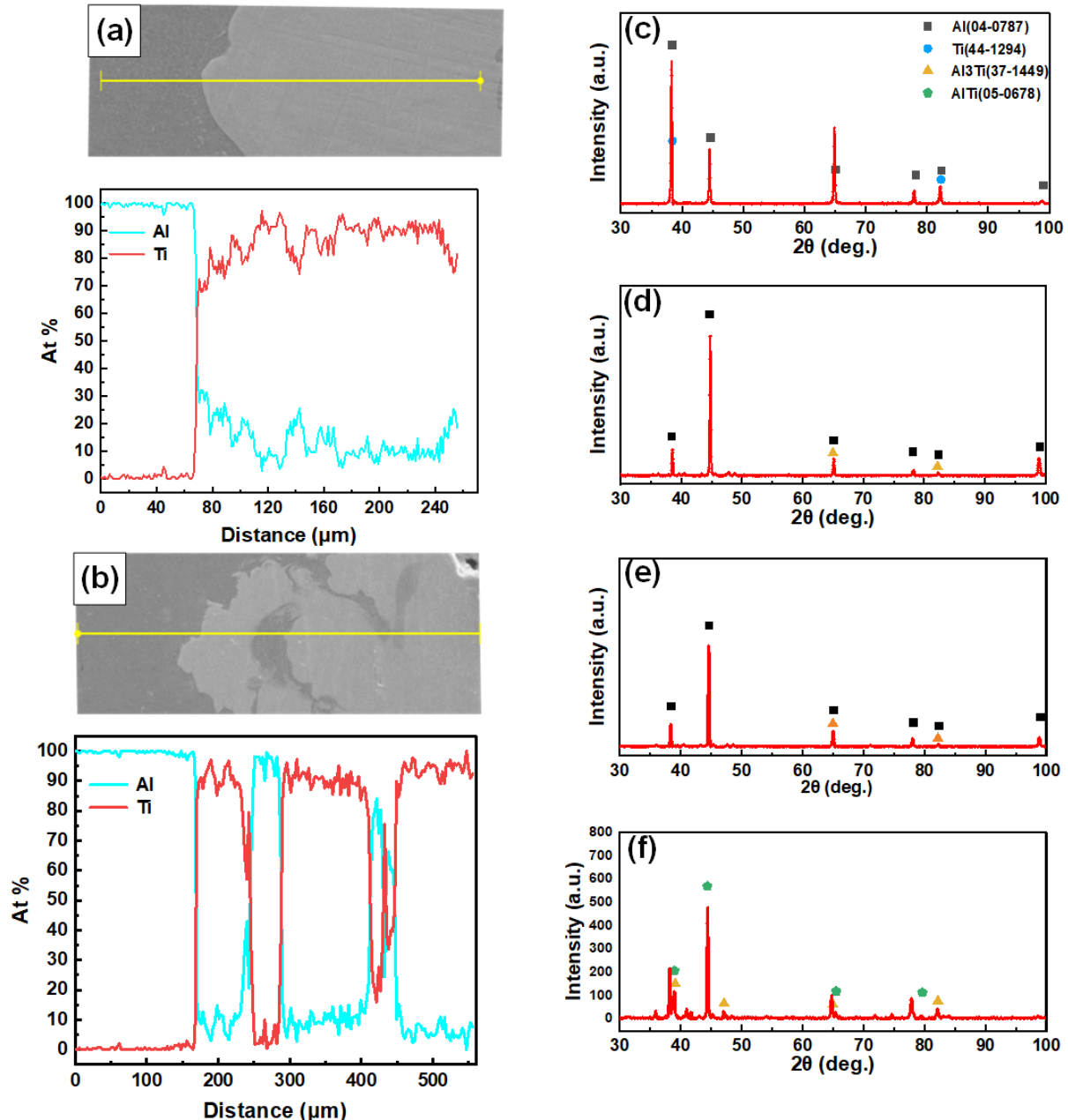

Fig. 10. EDS line scanning of state 2(a) and state 3(b). Mechanical bond and metallurgical bond can be observed. X-Ray Diffraction patterns of samples for the four states. (c) state 1, (d) state 2, (e) state 3, (f) state 4.

4.4 Mechanical properties of the joints

As shown in **Fig. 11**, for states 2,3,4 we stacked 26 layers of titanium wires on the substrate

for mechanical properties testing. The samples were wire-cut into 30 mm × 8mm × 1.5 mm sheets for tensile testing. **Fig. 12** shows the UTS for states 2, 3, and 4. The max tensile strength of state 3 were respectively 380.3 MPa, and the tensile strength reached 67.90% of the tensile strength of 7075 Al alloy T6 (560 MPa). While state 2 and state 4 only reached 28.89% and 36.85% of the 7075 Al alloy. This is because the heat input of state2 is not sufficient leading to the existence of part of the substrate melt pool is not deep enough, the wire is not well infiltrated in the wire melt pool, so the mechanical occlusion interface formed by the two metals cannot withstand the large tensile stress eventually fracture at the interface.
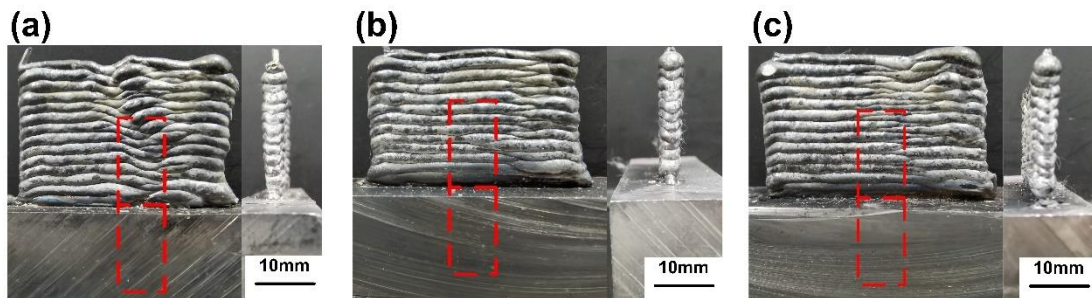

Fig. 11. Tensile test samples: (a) state 2; (b) state 3; (c) state 4.
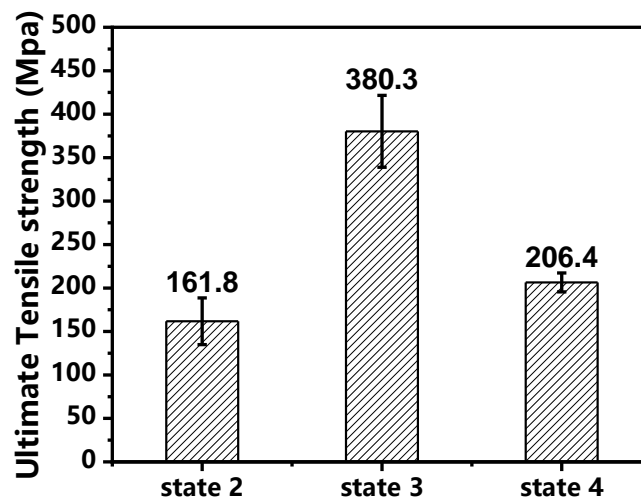
Fig.12. Ultimate tensile strength (UTS) for 3 states.

Fig. 13 displays the fracture behavior at the junction. Although states 2,3 and 4 all fracture at the interface junction, the fracture patterns presented are quite different. As shown in Fig.12(d) on the fracture surface of state 2, many tough nests can be found, indicating that the elongation of state2 should be the best of the four states. However, the microstructure of stare 2 shows that state 2 is not fully connected, which leads to poor interface fusion. In tensile experiments, stress concentration occurs, resulting in a lower elongation and tensile strength than in state3. Therefor the failure of state 2 is due to ductile fracture. From **Fig. 13**(f), it can be seen that the failure of state 4 is due to brittle fracture, since the fracture surface is relatively flat and perpendicular to the direction of the tensile stress and a clear crack can be observed. This is due to the excessive heat input that completely melts the titanium alloy resulting in the direct contact of the melt pool of both metals generating a large amount of brittle intermetallic compounds AlTi and Al3Ti. It can be concluded that FEWLAM does improve the performance of the connection between dissimilar metals through thermal modulation and mechanical occlusion.

Fig. 13. FEWLAM fracture analyses: micro-morphology of the fractured surface of state 2(a), state 3(b) and state4(c), (d-f) micro-morphology marked in (a-c).
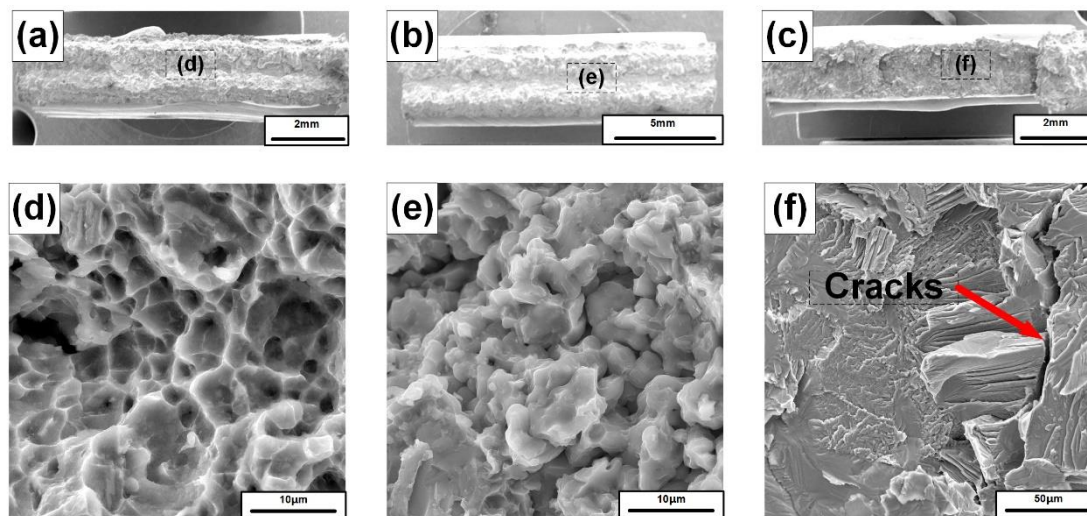
5. Conclusions

In this work, a new strategy called force enhanced wire laser dissimilar metal additive manufacturing was proposed. We have combined numerical simulations and experimental results to elucidate the mechanism of force enhancement on dissimilar metal joining interfaces, and validated the new method in terms of surface morphology, microstructure and mechanical properties. The results show that the proposed method provides a new approach for heterogeneous metal additive manufacturing, and some important findings are summarized as follows.

(1) The initial contact force between the filament and the substrate can enhance the heat transfer between the dissimilar metals, reduce the generation of defects in the transition zone, and improve the mechanical properties of the dissimilar metal interface.

(2) Thermal regulation was achieved by adjusting the treatment parameters to realize the combination of two interfaces of liquid filament-solid filament-liquid substrate, which effectively controls the generation of brittle compounds between dissimilar metals.

(3) Tensile experiments showed that the bonding strength between dissimilar species was indeed improved by controlling the formation of brittle compounds between Al and Ti alloys.

Acknowledgements

References

[1]   S. Cooke, K. Ahmadi, S. Willerth, R. Herring, Metal additive manufacturing: Technology, metallurgy and modelling, J. Manuf. Process. 57 (2020) 978–1003. https://doi.org/10.1016/j.jmapro.2020.07.025.

[2]   R. Shi, S.A. Khairallah, T.T. Roehling, T.W. Heo, J.T. McKeown, M.J. Matthews, Microstructural control in metal laser powder bed fusion additive manufacturing using laser beam shaping strategy, Acta Mater. 184 (2020) 284–305. https://doi.org/10.1016/j.actamat.2019.11.053.

[3]   M. Attaran, The rise of 3-D printing: The advantages of additive manufacturing

over traditional manufacturing, Bus. Horiz. 60 (2017) 677–688. https://doi.org/10.1016/j.bushor.2017.05.011.

[4]   C. Li, C.H. Fu, Y.B. Guo, F.Z. Fang, A multiscale modeling approach for fast prediction of part distortion in selective laser melting, J. Mater. Process. Technol. 229 (2015) 703–712. https://doi.org/10.1016/j.jmatprotec.2015.10.022.

[5]   T. DebRoy, H.L. Wei, J.S. Zuback, T. Mukherjee, J.W. Elmer, J.O. Milewski, A.M. Beese, A. Wilson-Heid, A. De, W. Zhang, Additive manufacturing of metallic components – Process, structure and properties, Prog. Mater. Sci. 92 (2018) 112–224. https://doi.org/10.1016/j.pmatsci.2017.10.001.

[6]   W.E. Frazier, Metal additive manufacturing: A review, J. Mater. Eng. Perform. 23 (2014) 1917–1928. https://doi.org/10.1007/s11665-014-0958-z.

[7]   C. Yan, L. Hao, A. Hussein, S.L. Bubb, P. Young, D. Raymont, Evaluation of light-weight AlSi10Mg periodic cellular lattice structures fabricated via direct metal laser sintering, J. Mater. Process. Technol. 214 (2014) 856–864. https://doi.org/10.1016/j.jmatprotec.2013.12.004.

[8]   F. Yan, W. Xiong, E.J. Faierson, Grain structure control of additively manufactured metallic materials, Materials (Basel). 10 (2017) 1260. https://doi.org/10.3390/ma10111260.

[9]   T.D. Ngo, A. Kashani, G. Imbalzano, K.T.Q. Nguyen, D. Hui, Additive manufacturing (3D printing): A review of materials, methods, applications and challenges, Compos. Part B Eng. 143 (2018) 172–196. https://doi.org/10.1016/j.compositesb.2018.02.012.

[10]   A. Bandyopadhyay, K.D. Traxel, Invited review article: Metal-additive manufacturing—Modeling strategies for application-optimized designs, Addit. Manuf. 22 (2018) 758–774. https://doi.org/10.1016/j.addma.2018.06.024.

[11]   B. Fu, G. Qin, F. Li, X. Meng, J. Zhang, C. Wu, Friction stir welding process of dissimilar metals of 6061-T6 aluminum alloy to AZ31B magnesium alloy, J. Mater. Process. Technol. 218 (2015) 38–47. https://doi.org/10.1016/j.jmatprotec.2014.11.039.

[12]   M. Aonuma, K. Nakata, Dissimilar metal joining of ZK60 magnesium alloy and titanium by friction stir welding, Mater. Sci. Eng. B Solid-State Mater. Adv. Technol. 177 (2012) 543–548. https://doi.org/10.1016/j.mseb.2011.12.031.

[13]   R. Prasad Mahto, S.K. Pal, Friction Stir Welding of Dissimilar Materials: An Investigation of Microstructure and Nano-Indentation Study, J. Manuf. Process. 55 (2020) 103–118. https://doi.org/10.1016/j.jmapro.2020.03.050.

[14]   S. Ravikumar, V. Seshagiri Rao, R. V. Pranesh, Effect of Process Parameters on Mechanical Properties of Friction Stir Welded Dissimilar Materials between AA6061-T651 and AA7075-T651 Alloys, Int. J. Adv. Mech. Eng. 4 (2014) 101–114.

[15]   P. Sadeesh, K.M. Venkatesh, V. Rajkumar, P. Avinash, N. Arivazhagan, R.K. Devendranath, S. Narayanan, Studies on friction stir welding of aa 2024 and aa 6061 dissimilar metals, Procedia Eng. 75 (2014) 145–149. https://doi.org/10.1016/j.proeng.2013.11.031.

[16]   A. Simar, State of the art about dissimilar metal friction stir welding, Sci. Technol. Weld. Join. 1718 (2016) 0–15. https://doi.org/10.1080/17432936.2016.1251712.

[17]   X. He, F. Gu, A. Ball, A review of numerical analysis of friction stir welding, Prog. Mater. Sci. 65 (2014) 1–66. https://doi.org/10.1016/j.pmatsci.2014.03.003.

[18]   C.F. Tey, X. Tan, S.L. Sing, W.Y. Yeong, Additive manufacturing of multiple

materials by selective laser melting: Ti-alloy to stainless steel via a Cu-alloy interlayer, Addit. Manuf. 31 (2020) 100970. https://doi.org/10.1016/j.addma.2019.100970.

[19]   X. Chen, Z. Lei, Y. Chen, Y. Han, M. Jiang, Z. Tian, J. Bi, S. Lin, Microstructure and tensile properties of Ti/Al dissimilar joint by laser welding-brazing at subatmospheric pressure, J. Manuf. Process. 56 (2020) 19–27. https://doi.org/10.1016/j.jmapro.2020.04.062.

[20]   Z. Lei, P. Li, X. Zhang, S. Wu, H. zhou, L. Nannan, Microstructure and mechanical properties of welding–brazing of Ti/Al butt joints with laser melting deposition layer additive, J. Manuf. Process. 38 (2019) 411–421. https://doi.org/10.1016/j.jmapro.2019.01.040.

[21]   Y. Chen, S. Chen, L. Li, Effects of heat input on microstructure and mechanical property of Al/Ti joints by rectangular spot laser welding-brazing method, Int. J. Adv. Manuf. Technol. 44 (2009) 265–272. https://doi.org/10.1007/s00170-008-1837-2.

[22]   H. Sahasrabudhe, R. Harrison, C. Carpenter, A. Bandyopadhyay, Stainless steel to titanium bimetallic structure using LENS™, Addit. Manuf. 5 (2015) 1–8. https://doi.org/10.1016/j.addma.2014.10.002.

[23]   M. Gao, S.W. Mei, Z.M. Wang, X.Y. Li, X.Y. Zeng, Characterisation of laser welded dissimilar Ti/steel joint using Mg interlayer, Sci. Technol. Weld. Join. 17 (2012) 269–276. https://doi.org/10.1179/1362171812Y.0000000002.

[24]   I. Tomashchuk, P. Sallamand, N. Belyavina, M. Pilloz, Evolution of microstructures and mechanical properties during dissimilar electron beam welding of titanium alloy to stainless steel via copper interlayer, Mater. Sci. Eng. A. 585 (2013) 114–122. https://doi.org/10.1016/j.msea.2013.07.050.

[25]   S. Zhao, G. Yu, X. He, Y. Hu, Microstructural and mechanical characteristics of laser welding of Ti6Al4V and lead metal, J. Mater. Process. Technol. 212 (2012) 1520–1527. https://doi.org/10.1016/j.jmatprotec.2012.02.014.

[26]   C. Yao, B. Xu, X. Zhang, J. Huang, J. Fu, Y. Wu, Interface microstructure and mechanical properties of laser welding copper-steel dissimilar joint, Opt. Lasers Eng. 47 (2009) 807–814. https://doi.org/10.1016/j.optlaseng.2009.02.004.

[27]   Y. Hu, X. He, G. Yu, Z. Ge, C. Zheng, W. Ning, Heat and mass transfer in laser dissimilar welding of stainless steel and nickel, Appl. Surf. Sci. 258 (2012) 5914–5922. https://doi.org/10.1016/j.apsusc.2012.02.143.

[28]   R. Borrisutthekul, T. Yachi, Y. Miyashita, Y. Mutoh, Suppression of intermetallic reaction layer formation by controlling heat flow in dissimilar joining of steel and aluminum alloy, Mater. Sci. Eng. A. 467 (2007) 108–113. https://doi.org/10.1016/j.msea.2007.03.049.

[29]   W. Huang, H. Wang, T. Rinker, W. Tan, Investigation of metal mixing in laser keyhole welding of dissimilar metals, Mater. Des. 195 (2020) 109056. https://doi.org/10.1016/j.matdes.2020.109056.

[30]   M.S. Rahman, P.J. Schilling, P.D. Herrington, U.K. Chakravarty, A Comparison of the Thermo-Fluid Properties of Ti-6Al-4V Melt Pools Formed by Laser and Electron-Beam Powder-Bed Fusion Processes, J. Eng. Mater. Technol. Trans. ASME. 143 (2021) 1–13. https://doi.org/10.1115/1.4048371.

[31]   J. Du, X. Wang, H. Bai, G. Zhao, Y. Zhang, Numerical analysis of fused-coating metal additive manufacturing, Int. J. Therm. Sci. 114 (2017) 342–351. https://doi.org/10.1016/j.ijthermalsci.2017.01.011.